Ultrawide-view achromatic circular polarization dynamic converter using an easy-to-integrate multi-layer structure

YANG YU,[1,2,3] (iD) **ZIJUN SUN,**[1,2,3] **QUANQUAN MU,**[1,2,4]
QIDONG WANG,[1,2,5] **CHENGLIANG YANG,**[1,2] **ZENGHUI PENG,**[1,2]
SHIXIAO LI,[1,2,3] **AND ZEKUN BI**[1,2,3]

[1]*State Key Laboratory of Applied Optics, Changchun Institute of Optics, Fine Mechanics and Physics, Chinese Academy of Sciences, Changchun 130033, China*
[2]*Key Laboratory of Optical System Advanced Manufacturing Technology, Chinese Academy of Sciences, Changchun 130033, China*
[3]*University of Chinese Academy of Sciences, Beijing 10049, China*
[4]*muquanquan@ciomp.ac.cn*
[5]*qdwang@ciomp.ac.cn*

Abstract: What we believe to be a novel integrated circular polarization dynamic converter (CPDC) is proposed based on the four-layer mirror symmetry structure. By designing the twisted structure and rearranging the orientation direction of liquid crystal molecules for each layer, the application wavelength range could be broadened. For the viewing angle expansion, negative birefringent films are selected to compensate for the retardation deviation under oblique incidence. Finally, the particle swarm algorithm is used to optimize the whole configuration, and the polarization conversion efficiency calculated by the finite element method (FEM) can achieve 90% in the wavelength range from 320 nm to 800 nm at an ultrawide view of 160°. Compared with traditionally active liquid crystal waveplates, the design has potential advantages in both wavelength and field of view (FOV) and provides the possibility for the integrated and flimsy fabrication of devices.

1. Introduction

Liquid crystal optical devices have the ability to dynamically modulate the polarization state and geometric phase of light [1,2] in real time, offering the possibility of "dynamic reconstruction" for optical systems, which is very important for non-mechanical beam regulation [3–5], LiDAR [6], metasurface structure [7,8], vector beam regulation [9,10] and virtual reality display [11–13] applications. The active polarization converter is one of the most commonly used devices in many scenarios, and its polarization conversion efficiency, especially under conditions of a large FOV and wide wavelength range, directly determines the performance of optical systems.

In previous studies, liquid crystal devices based on ECB mode or TN mode were usually used as typical active polarization converters, and many researchers have also been conducted to optimize the FOV and wavelength range characteristics of these two structures [14–18]. In 2004, Lavrentovich et al introduced a broadband halfwave retarder with a sandwich structure, which has a parallel alignment LC cell arranged between two twisted nematic LC cells, for normal incident light from 400 nm to 700 nm [16]. When a sufficiently high voltage is applied to all three layers, the device produces a near-zero effect on the incident polarization, which exhibits the activated and quiescent states. In 2021, Xiong et al. introduced a CPDC consisting of a TN cell and two achromatic quarter-wave plates (AQW), which has a conversion efficiency of over 90% for the incident light in 465 – 630 nm and ±30° FOV [17]. Although the twisted nematic liquid crystal has wide usage in many scenarios with good performance in broadband modulation

and agile electric-response characteristics [18,19], it has drawbacks in the symmetry of FOV inevitably, which is mainly caused by the difference between voltage-on state and voltage-off state. In the same year, Chen et al. introduced a circular polarization converter with a mirror symmetry structure, which is very useful for geometric phase devices, such as polarization gratings. In the normal incident case, the diffraction efficiency is over 99% in 420 - 945 nm, and in the oblique incident case, the diffraction efficiency is over 90% in the range of ±30° [20]. However, it is a passive structure that cannot achieve dynamic switching of polarization states. Compensation film "+c film" was used to expand the viewing angle based on the three-layer QHQ model [21], the structure will inevitably lead to a decrease in the transmittance of the device due to the increase of the substrates. Moreover, the deviation of the optical axis angles will also lead to a decrease in the conversion efficiency, affecting its field of view effect and band effect.

Under this circumstance, an ultrawide FOV and broadband CPDC which is easy for realizing the integration is introduced in this paper. It provides a submillisecond response speed because of the fast switching of electrically suppressed helix ferroelectric liquid crystal (ESHFLC) molecules, which is an ideal choice for dynamic modulation applications [21–23]. In addition, the in-plane optical axis reversal characteristic helps to achieve consistent FOV performance in both operating states. The basic principles and configuration are introduced in the second section. Finally, we optimized its structure parameters, evaluated its wavelength range and FOV performance, and compared it with several traditional polarization converters.

2. Basic principles of the CPDC

Referring to the symmetry of orthogonal polarization states and the achromatic principles, a four-layer mirror symmetric structure is adopted as the basic structure of the converter [20]. Its basic structure mainly consists of a pair of single twisted LC layers (T1, T2), a parallel-oriented LC layer (H1), and an ESHFLC switching layer (H2), shown in Fig. 1(a-c). According to the symmetry principle, twisted LC layers are used to convert the polarization state of light back and forth between circular polarization (initial and termination states) and linear polarization (intermediate polarization states). The parallel-oriented layer and ESHFLC layer accomplish the dynamic switching progress of the intermediate states and reverse the polarization dispersion at the same time. The conversion process of the twisted liquid crystal layers can be explained by the 3×3 Muller matrix calculation [24,25]. $\mathbf{T}_m$ could represent the twisted layers as:

$$\mathbf{T}_m = \mathbf{R}(-\varphi_m)\mathbf{R}(-\Phi_m)\mathbf{M}_m\mathbf{R}(\varphi_m) \tag{1}$$

The polarization conversion of the twisted layer is determined by the formula: $\mathbf{S}_o(\lambda) = \mathbf{T}_m \cdot \mathbf{S}_i(\lambda)$, where $\mathbf{S}_o(\lambda)$ and $\mathbf{S}_i(\lambda)$ are wavelength-dependent output and input Stokes vectors, respectively. $\mathbf{R}_m$ is the rotation matrix, determined by the following equation:

$$\mathbf{R}(\Phi_m) = \begin{pmatrix} \cos(2\Phi_m) & \sin(2\Phi_m) & 0 \\ -\sin(2\Phi_m) & \cos(2\Phi_m) & 0 \\ 0 & 0 & 1 \end{pmatrix} \tag{2}$$

$\mathbf{M}_m$ is determined by the following equation:

$$\mathbf{M}_m = \begin{pmatrix} 1 - 2\frac{\Phi_m^2}{X^2}\sin^2 X & \frac{\Phi_m}{X}\sin(2X) & \frac{\Phi_m\Gamma}{X^2}\sin^2 X \\ -\frac{\Phi_m}{X}\sin(2X) & \cos(2X) & \frac{\Gamma}{2X}\sin(2X) \\ \frac{\Phi_m\Gamma}{X^2}\sin^2 X & -\frac{\Gamma}{2X}\sin(2X) & 1 - 2\frac{\Gamma^2}{(2X)^2}\sin^2 X \end{pmatrix} \tag{3}$$

φ is the orientation angle of LCs for each layer; Φ_m represents the twisted angle; d represents the liquid crystal layer thickness. $\Gamma = 2\pi\Delta nd/\lambda$ is the phase delay, Δn is birefringence, λ is
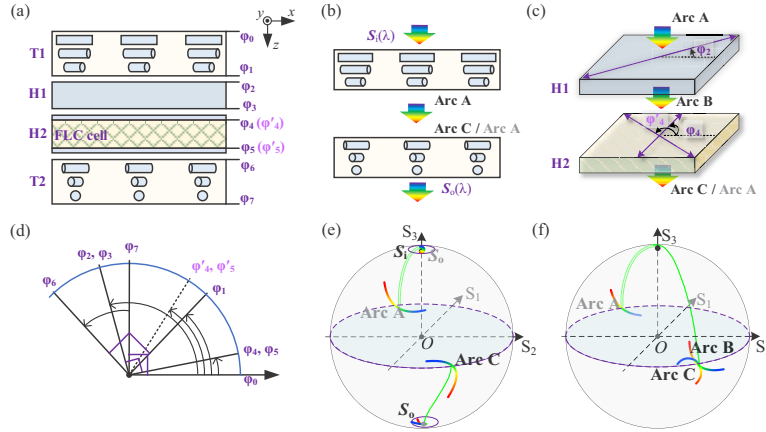
Fig. 1. Principles of the broadband CPDC. (a) The basic structure of the ESHFLC-based CPDC; (b) Twisted structures; (c) Polarization switching principle; (d) The orientation direction of LC at each interface; (e) Polarization evolution trajectories of twisted layers; (f) Polarization evolution trajectories of switchable combination layers. (T1: $S_i \rightarrow$ Arc A, H1: Arc A $\rightarrow$ Arc B, H2: Arc B$\rightarrow$ Arc C or Arc B$\rightarrow$ Arc A, T2: Arc C $\rightarrow S_o$ or Arc A $\rightarrow S_i$).

the wavelength, and $X = (\Phi_m{}^2 + (\Gamma/2)^2)^{1/2}$. The chiral rotation is defined as: $\Phi_m > 0$ for the left-handed helix and $\Phi_m < 0$ for the right-handed helix.

The polarization dispersion of twisted layers with chiral symmetric structures on the northern and southern parts of the Poincaré sphere is exactly complementary according to the previous study of twisted layers [20]. However, in order to dynamically convert the polarization state between circular polarization (initial and termination states) and linear polarization (intermediate polarization states), it is necessary to transform the mirror-symmetric twisted structure. The inverse matrix of a twisted layer is expressed as $\mathbf{T}^{-1}{}_m$:

$$\mathbf{T}^{-1}{}_m = \mathbf{R}(-\varphi_m)\mathbf{M}^{-1}{}_m\mathbf{R}(\Phi_m)\mathbf{R}(\varphi_m) \tag{4}$$

The Muller matrix of a twisted liquid crystal layer which is mirror-symmetric about the twisted layer and rotated 90° along the normal direction is denoted as $\mathbf{T'}_m$:

$$\mathbf{T'}_m = \mathbf{R}(-\varphi_m)\mathbf{R}\left(-\frac{\pi}{2}\right)\mathbf{M'}_m\mathbf{R}\left(\frac{\pi}{2}\right)\mathbf{R}(\Phi_m)\mathbf{R}(\varphi_m) \tag{5}$$

$$\mathbf{T'}_m = \mathbf{R}(-\varphi_m)\begin{pmatrix} 1-2\frac{\Phi_m{}^2}{X^2}\sin^2 X & -\frac{\Phi_m}{X}\sin(2X) & \frac{\Phi_m\Gamma}{X^2}\sin^2 X \\ \frac{\Phi_m}{X}\sin(2X) & \cos(2X) & -\frac{\Gamma}{2X}\sin(2X) \\ \frac{\Phi_m\Gamma}{X^2}\sin^2 X & \frac{\Gamma}{2X}\sin(2X) & 1-2\frac{\Gamma^2}{(2X)^2}\sin^2 X \end{pmatrix}\mathbf{R}(\Phi_m)\mathbf{R}(\varphi_m) \tag{6}$$

Here, $\mathbf{M}_m$ is a real unitary matrix, so we have $\mathbf{M}^{-1}{}_m = \mathbf{M}^{\dagger}{}_m = \mathbf{M}^T{}_m$ [25]. $\mathbf{M}^T{}_m$ is the transposed matrix, $\mathbf{M}^{\dagger}{}_m$ is the hermitian conjugate matrix. It is obvious that $\mathbf{T'}_m = \mathbf{T}^{-1}{}_m$, when the polarization state $S_o(\lambda)$ is incident on this twisted liquid crystal layer, the output polarization states is $S_i(\lambda) = \mathbf{T}^{-1}{}_m \cdot S_o(\lambda) = \mathbf{T'}_m \cdot S_o(\lambda)$. Besides, the output polarization states are always orthogonal after the orthogonal polarization states pass through the twisted liquid crystal layer. $S_i(\lambda)$ and $-S_i(\lambda)$ are orthogonal polarization states apparently, when the polarization light $-S_i(\lambda)$ passes through the twisted layer, the output polarization can be expressed as:

$$\mathbf{S'_o}(=\lambda) = \mathbf{T}_m \times [-\mathbf{S_i}(\lambda)] = -\mathbf{T}_m \times \mathbf{S_i}(\lambda) = -\mathbf{S_o}(\lambda) \tag{7}$$

The above matrix derivation process could well explain how the dynamically converting process between linear polarization and circular polarization is accomplished.

According to the optic-axis reversal characteristic of the ESHFLC layer, the intermediate polarization state can be switched from Arc A to Arc C or maintained in Arc A as shown in Fig. 1(f), which corresponds to the polarization states on the Poincaré sphere. The orientation direction $\varphi_{i(i=0,1,2,...,7)}$ of LC at each interface of all layers is shown in Fig. 1(d). The Poincaré sphere model in Fig. 1(e-f) shows the polarization evolution process of the ESHFLC-based CPDC. For incident right circularly polarized light with a certain bandwidth, the initial state is represented as S_i. After passing through the T1 layer, the polarization state is changed to Arc A. The H1 layer acts as a halfwave plate and rotates Arc A to Arc B. For the converting state, the ESHFLC layer is used to convert the polarization state distribution from Arc B to Arc C, and ultimately to S_o under the modulation of T2 layer. For the non-converting state, the ESHFLC layer is used to convert the polarization state distribution from Arc B back to Arc A and return to the initial state S_i under the modulation of T2 layer. The H1 and H2 combination also has the ability to reverse the dispersion during polarization modulation, which is very useful for dispersion compensation.

To evaluate the performance of the CPDC device, the polarization conversion efficiency (PCE) based on the normalized Stokes vector $S = (S_1, S_2, S_3)$ is used. For ideal circularly polarized light, the value S_3 is equal to ± 1. During the polarization conversion process, the actual polarization state will gradually deviate from the ideal value due to the influence of wavelength dispersion and different FOV. The wavelength and FOV-related PCE can be expressed as:

$$\eta(\lambda, \theta, \varphi) = \frac{1 + |S_3|}{2} \times 100\% \tag{8}$$

where λ represents the wavelength of the incident light, θ and φ represent the incident angle and the azimuth angle of the incident light, respectively.

To achieve excellent wavelength range performance, it is necessary to optimize the thickness of each layer and the orientation direction of LC at each interface. The Poincaré sphere model [16] is used for real-time monitoring and evaluation of its performance for optimization. The simulated refractive index parameters of each LC layer in this paper are considered under a small birefringence condition with $\Delta n = 0.1$, $n_e = 1.6$, $n_o = 1.5$. For circularly polarized light in the wavelength range of 300-900 nm under normal incidence, the optimization results are shown in Table 1. The φ_f and φ_r represent the LC orientation direction at the front and rear interfaces of each LC layer respectively, and Φ is the twist angle. The polarization evolution trajectory for the switching process is portrayed on the Poincaré sphere, shown in Fig. 2(a), which indicates that the optimized structure can achieve uniform compensation for light dispersion. Then we calculated the wavelength-dependent PCE using the FEM method, and the results indicate that the PCE achieves over 90% in 380-870 nm for both converting and non-converting states under normal incidence. Besides, the bandwidth shrinks with the increase of the PCE for the converting state, but the non-converting state maintains excellent performance before the FOV compensation, the PCE maintains close to 100% for the whole 300-900 nm waveband, which is shown in Fig. 2(b).

Table 1. Basic broadband CPDC design

Layer	T1	H1	FLC	T2
d (µm)	1.60	2.66	2.66	1.60
φ_f (°)	0.40	110.30	43.90 ± 22.90	140.60
φ_r (°)	51.50	110.30	43.90 ± 22.90	89.40
Φ (°)	51.10	-	-	-51.20

The FOV-PCE polar diagrams under three different central wavelengths (460 nm, 530 nm, and 630 nm) in the visible spectrum are shown in Fig. 3, and the calculation results indicate that the PCE can exceed 90% while the FOV is not more than $\pm 40°$ for both working states. The
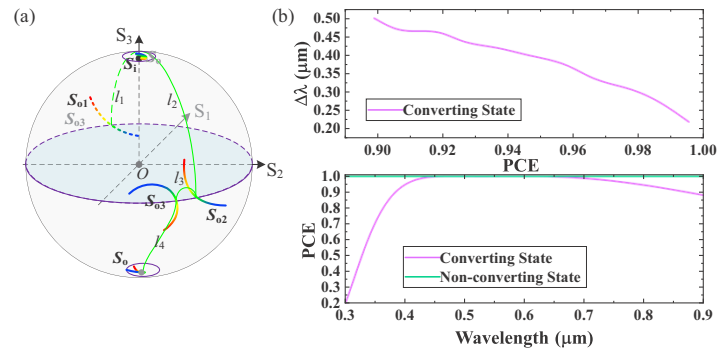
Fig. 2. (a) Switching process on the Poincaré sphere. (b) The wavelength-PCE curves of the broadband CPDC.

optimized broadband CPDC displays exceptional optical characteristics in a limited FOV, which meets the FOV requirement of most optical systems. However, for diffractive optical systems with larger and higher efficiency requirements, we still need to further improve the CPDC's performance.
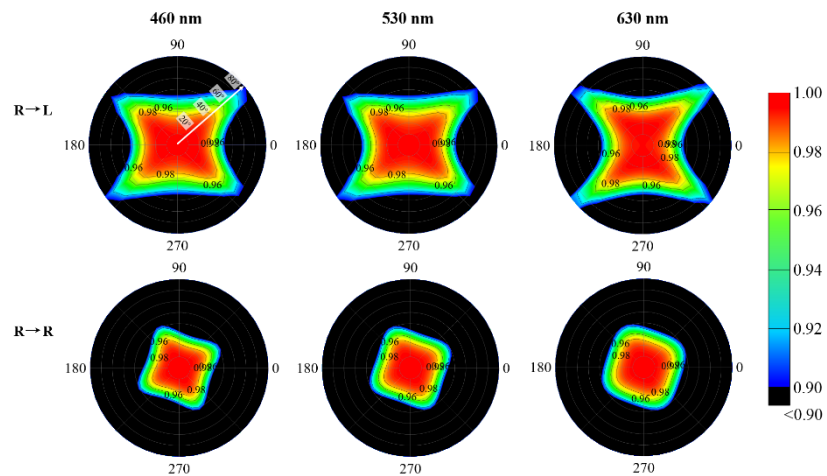

Fig. 3. The FOV-PCE polar diagrams of the broadband CPDC.

3. Optimization of the FOV

In order to expand the FOV of the CPDC device and get a higher PCE, we further designed the H1 and H2 layers of the basic configuration. They are all divided into a combination of positive and negative birefringent retardation layers, and these different birefringent films have the opposite polarization evolution trajectories on the Poincaré sphere (usually clockwise for the positive birefringent film and counterclockwise for the negative birefringent film). The FOV compensation depends on the orientation of LC molecules and the optical delay of each retardation film, and some restrictions must be complied with for the reform of the layers. The reformed CPDC should not affect the wavelength range performance under normal incidence, so the LC orientation direction and the thickness of each LC layer are strictly limited and carefully modified.

We carried out different retardation film combination designs and selected the optimal FOV compensation method for structural optimization, then a combination of a negative birefringent film (NH1) with λ/8 retardation and a positive birefringent film H1 with 3λ/8 retardation was selected to decrease the retardation deviation caused by the simplex half-wave delay layer under different FOV angles. Two negative birefringent films (NH2, NH3) with λ/8 retardation are used for reforming H2 layer, because H2 is an FLC cell, and its optical axis switches in-plane under the drive of an electric field. As a result, the compensation films are arranged without influencing the converting and the achromatic characteristic as shown in Fig. 4. To obtain better performance of the wide band, the particle swarm algorithm was used to optimize all the angle and thickness parameters, and the optimized results are shown in Table. 2, where φ_f and φ_r represent the LC orientation direction at the front and rear interfaces of each LC layer respectively, and Φ is the twist angle.

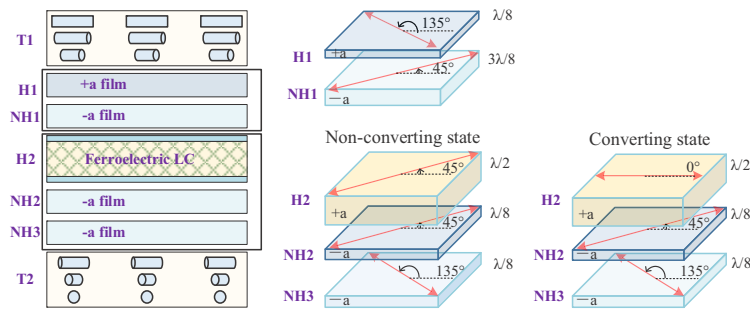**Fig. 4.** Schematic diagram of the ultrawide view and broadband CPDC.

Table 2. Ultrawide-view and broadband CPDC design

Layer	T1	H1	NH1	FLC	NH2	NH3	T2
d (µm)	1.18	0.40	2.17	2.40	0.8	0.8	0.9
φ_f (°)	-2.00	131.00	17.20	53.10 ± 23.20	57.50	164.0	150.0
φ_r (°)	27.00	131.00	17.20	53.10 ± 23.20	57.50	164.0	115
Φ (°)	29.00	-	-	-	-	-	-35

The CPDC has a very comprehensive performance, which not only ensures the high efficiency of different wavebands at a small incident angle, but also considers the performance of different incident angles at the same waveband. The FOV-PCE calculation results within ±80° are shown in Fig. 5. The results indicate that under ±80° FOV condition, the PCE of the three central wavelengths for both the converting state and the non-converting state is all greater than 90%. If the viewing angle is required to be within ±45°, the PCE will be over 98% in the whole FOV. To evaluate the wide-band performance of the structure after FOV compensation, the wavelength-PCE curves are portrayed in Fig. 6, and the PCE of the non-converting state after FOV compensation is totally over 95% for the whole 300-900 nm waveband. The orthogonal circularly polarized conversion of light in 320-800 nm can reach more than 90% PCE, which suggests that the FOV widen strategies do not shrink the application bandwidth compared with the waveband results in Fig. 2(b). In addition, the FOV performance curves of the designed CPDC at the worst azimuth angle were selected and compared with the traditional PA cell and TN cell polarization converters, as shown in Fig. 7. The results demonstrate that the CPDC performance is superior, especially for the central FOV, which is very beneficial for the precise beam steering system.
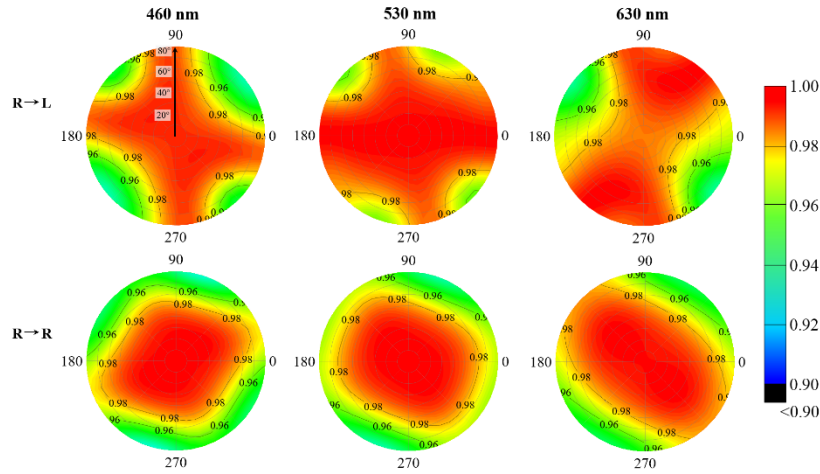
Fig. 5. The FOV-PCE polar diagrams of the ultrawide-view and broadband CPDC.
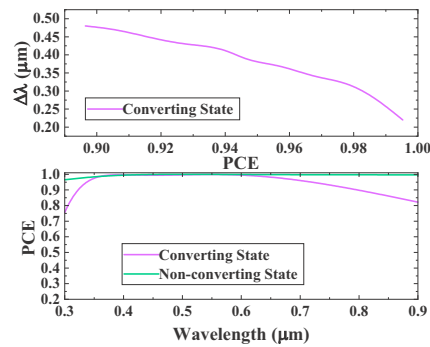

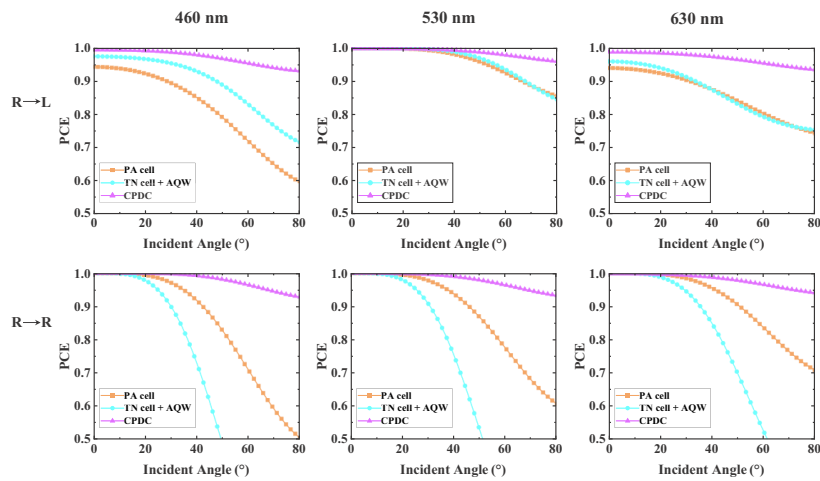**Fig. 6.** The wavelength-PCE curves of the ultrawide-view and broadband CPDC.

Fig. 7. The FOV-PCE curves of three different polarization converters.

4. Conclusion

The proposed CPDC with composite structure provide a new method for the integrated polarization-switching elements, and can significantly improve the waveband and FOV performance. Compared with the configuration in previous work [21], the CPDC designed in this paper can achieve more than 90% circular polarization conversion efficiency in 320-800 nm and ±80° FOV, although the previous configuration gives 97% high conversion efficiency, it is limited within 400-700 nm band and ±45° FOV. The broadband property is improved because of the twisted layer, on the other hand, there will be more freedom to optimize the structure because of the increased compensation films, but the cost and fabrication difficulty will also increase. Moreover, the new CPDC provides the possibility to use liquid crystal polymers to spincoat multilayer structures, which obtains better optical surface quality and uniformity and achieves accurate control of thickness and angle parameters. Compared with simplex polarization converters, the CPDC design can make the geometric phase-based optical device more advantageous in various optical scenarios.

Disclosures. The authors declare no conflicts of interest.

Data Availability. No data were generated or analyzed in the presented research.

References

1. J. Anandan, "The geometric phase," Nature **360**(6402), 307–313 (1992).
2. D. H. Goldstein, *Polarized light*, 3rd ed. (CRC, 2017).
3. J. H. Xiong, Q. Yang, Y. N. Q. Li, *et al.*, "Holo-imprinting polarization optics with a reflective liquid crystal hologram template," Light: Sci. Appl. **11**(1), 54 (2022).
4. J. H. Xiong and S. T. Wu, "Planar liquid crystal polarization optics for augmented reality and virtual reality: from fundamentals to application," eLight **1**(1), 3 (2021).
5. J. Kim, C. Oh, S. Serati, *et al.*, "Wide-angle, nonmechanical beam steering with high throughput utilizing polarization gratings," Appl. Opt. **50**(17), 2636–2639 (2011).
6. K. Gao, H. H. Cheng, A. Bhowmik, *et al.*, "Nonmechanical zoom lens based on the Pancharatnam phase effect," Appl. Opt. **55**(5), 1145–1150 (2016).
7. Y. N. Q. Li, Z. Y. Luo, and S. T. Wu, "High-precision beam angle expander based on polymeric liquid crystal polarization lenses for LiDAR applications," Dig. Tech. Pap. - Soc. Inf. Disp. Int. Symp. **53**(1), 283–286 (2022).
8. N. Yu and F. Capasso, "Flat optics with designer metasurfaces," Nat. Mater. **13**(2), 139–150 (2014).
9. D. Lin, P. Y. Fan, E. Hasman, *et al.*, "Dielectric gradient metasurface optical elements," Science. **345**(6194), 298–302 (2014).
10. P. Z. Sun, B. H. Liu, Y. F. Wang, *et al.*, "Ultra-broadband multichannel vector vortex beams with versatile electrically-induced functionality," Laser Photonics Rev. **17**(9), 2300098 (2023).
11. Q. Yang, Y. N. Q. Li, Y. Q. Ding, *et al.*, "Compact foveated AR displays with polarization selective planar lenses," ACS Appl. Opt. Mater. (2023)
12. K. Yin, E. L. Hsiang, J. Y. Zou, *et al.*, "Advanced liquid crystal devices for augmented reality and virtual reality displays: Principles and Applications," Light Sci. Appl. **11**(1), 161 (2022).
13. S. Moon, C. K. Lee, S. W. Nam, *et al.*, "Augmented reality near-eye display using Pancharatnam-Berry phase lenses," Sci. Rep. **9**(1), 6616 (2019).
14. S. Pancharatnam, "Achromatic combinations of birefringent plates," Proc. - Indian Acad. Sci., Sect. A **41**(4), 137–144 (1955).
15. L. S. Li and M. J. Escuti, "Super achromatic wide-angle quarter-wave plates using multi-twist retarders," Opt. Express **29**(5), 7464–7478 (2021).
16. M. D. Lavrentovich, T. A. Sergan, and J. R. Kelly, "Switchable broadband achromatic half-wave plate with nematic liquid crystals," Opt. Lett. **29**(12), 1411–1413 (2004).
17. J. H. Xiong, Y. N. Q. Li, K. Li, *et al.*, "Aberration-free pupil steering Maxwellian display with wide-view broadband polarization converters," J. Soc. Inf. Disp. **29**(5), 298–304 (2021).
18. P. Z. Sun, B. H. Liu, X. Liu, *et al.*, "Ultra-broadband holography in visible and infrared regions with full-polarization nondispersive response," Opt. Lett. **48**(11), 3083–3086 (2023).
19. B. H. Liu, C. L. Yuan, H. L. Hu, *et al.*, "Dynamically actuated soft heliconical architecture via frequency of electric fields," Nat. Commun. **13**(1), 2712 (2022).
20. W. Chen, Y. Yu, Q. Q. Mu, *et al.*, "Super-broadband geometric phase devices based on circular polarization converter with mirror symmetry," Appl. Phys. Lett. **119**(10), 1–5 (2021).
21. Y. Yu, Z. B. Sun, Q. Q. Mu, *et al.*, "Design of a high-speed circular polarization converter with a large field of view and wavelength range," Opt. Express **31**(4), 6615–6622 (2023).

22. Y. Ma, X. Y. Liu, J. T. Sun, *et al.*, "Ferroelectric liquid crystal devices on strengthened photoalignment films," Liq. Cryst. **47**(10), 1452–1457 (2020).
23. C. T. Wang, A. Tam, C. L. Meng, *et al.*, "Voltage-controlled liquid crystal Pancharatnam–Berry phase lens with broadband operation and high photo-stability," Opt. Lett. **45**(19), 5323–5326 (2020).
24. D. K. Yang and S. T. Wu, *Fundamentals of Liquid Crystal Devices*, 2nd ed. (John Wiley & Sons, 2015).
25. R. A. Chipman, W. S. T. Lam, and G. Young, *Polarized light and optical systems*, 1st ed. (CRC, 2018).